

CO COMPONENT ESTIMATION BASED ON THE INDEPENDENT COMPONENT ANALYSIS

KIYOTOMO ICHIKI¹, RYOHEI KAJI², HIROAKI YAMAMOTO², TSUTOMU T. TAKEUCHI², YASUO FUKUI²

Draft version March 4, 2013

ABSTRACT

Fast Independent Component Analysis (FastICA) is a component separation algorithm based on the levels of non-Gaussianity. Here we apply the FastICA to the component separation problem of the microwave background including carbon monoxide (CO) line emissions that are found to contaminate the PLANCK High Frequency Instrument (HFI) data. Specifically we prepare 100GHz, 143GHz, and 217GHz mock microwave sky maps including galactic thermal dust, NANTEN CO line, and the Cosmic Microwave Background (CMB) emissions, and then estimate the independent components based on the kurtosis. We find that the FastICA can successfully estimate the CO component as the first independent component in our deflection algorithm as its distribution has the largest degree of non-Gaussianity among the components. By subtracting the CO and the dust components from the original sky maps, we will be able to make an unbiased estimate of the cosmological CMB angular power spectrum.

1. INTRODUCTION

Precise measurements of the Cosmic Microwave Background (CMB) anisotropies have been a powerful probe into the early universe and cosmology. Experiments such as COBE (Bennett et al. 1996), BOOMERanG (MacTavish et al. 2006), WMAP (Komatsu et al. 2011) have already placed strong constraints on the parameters of the cosmological model, such as the age of the universe, baryon and cold dark matter densities and so on. The third generation CMB satellite, PLANCK (Tauber et al. 2010), is expected to release its cosmological results soon which will include constraints on the amplitude of primordial gravitational waves, the spectral index and its running of the primordial curvature perturbations, the amount of primordial non-Gaussianity and so on, and thereby will give constraints on physics of the early universe such as inflation.

Such cosmological information can be obtained only when sources of uncertainty are removed successfully. With recent high-resolution and sensitive instruments, the main source of uncertainty is the contamination by foreground emissions from the Galaxy, rather than the instrumental noise itself. Therefore component separation methods have been progressively developed so far based on the analyses of data at different frequencies and different dependencies on frequency of the astrophysical emission laws (for a recent review, see Dunkley et al. (2009)). The methods include template fitting (Efstathiou et al. 2009; Katayama & Komatsu 2011), Internal Linear Combination (Eriksen et al. 2004), Correlated Component Analysis (Bonaldi et al. 2006), Maximum Entropy Method (Hobson et al. 1998) and so on, where the differences are in the way how they model the data and the assumptions made on the foreground components.

Along with the synchrotron and thermal dust emissions which constitute substantial portion of the foreground component of the Galaxy at microwave frequencies, it now becomes clear that the rotational transitions of carbon monoxide (CO) significantly contaminate the PLANCK observing bands (Planck HFI Core Team et al. 2011). In particular, the frequencies of the lowest two rotational transitions of CO, namely J=(1-0) and J=(2-1), are at the first and third transmis-

sion bands of PLANCK's High Frequency Instrument (HFI), that is, at 100 and 217 GHz bands. Therefore we must develop a method to remove this contribution for cosmological analysis.

A simple way to remove such contribution may be to use a template with help from the other CO line surveys, such as Columbia survey (e.g., Dame et al. (2001)) and NANTEN Galactic Plane Survey (NGPS) survey by NANTEN telescope (Onishi et al. 2001; Mizuno & Fukui 2004). However, these surveys are dedicated mainly to the Galactic plane where the most of the molecular clouds has been found and there has been no full sky CO map to be compared with the PLANCK full sky data. Therefore it will be helpful to find a method to obtain (even rough) information about the distribution of the CO molecular clouds, especially at high galactic latitudes, from the PLANCK data alone.

To this end we consider a fast component separation method to extract the CO distribution based on the Independent Component Analysis (FastICA) (Hyvärinen & Oja 1997). The FastICA has several advantages in comparison with the methods mentioned above; among them the most important point is that FastICA method needs no prior assumptions about the distribution of the foreground components and their frequency dependences (therefore it is called as Blind Source Separation in the statistics community). Instead the method uses statistical independency to separate the components as described below shortly. Therefore the method may be suitable to estimate the distribution at the current moment when we do not know much about the CO distribution on the full sky and its relative contributions to the PLANCK observing bands. Several applications of the FastICA to the CMB component separation problem can be found in the literature, which includes applications to the COBE (Maino et al. 2002, 2003), BEAST (Donzelli et al. 2006) WMAP data (Maino et al. 2007; Bottino et al. 2010) and simulated 21 cm maps (Chapman et al. 2012). Here we first apply the method to extract the CO component assuming the PLANCK HFI and evaluate its performance by means of Monte Carlo simulations, in terms of the angular power spectrum of temperature anisotropies which is one of the most important statistic for cosmological analysis.

2. FASTICA METHOD

ICA assumes that observed maps are given by a superposition of independent astrophysical components and the cosmo-

¹ Kobayashi-Maskawa Institute for the Origin of Particles and the Universe, Nagoya University, Nagoya 464-8602, Japan

² Department of Physics and Astrophysics, Nagoya University, Nagoya 464-8602, Japan

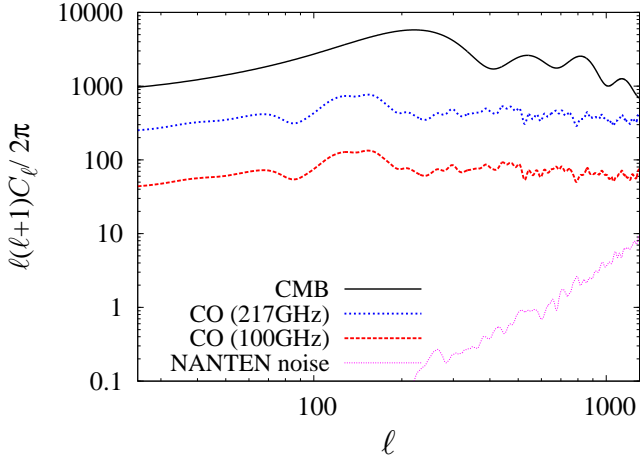


FIG. 1.— Angular power spectra of CO line emissions at the 100GHz band in the MBM and Pegasus region observed by the NANTEN telescope with estimated error magnitude (red dashed line). 217GHz signal is estimated assuming the line ratio of Ingalls et al. (2000) (blue dotted line). CO angular power spectrum gives more significant contribution at smaller angular scales relative to the cosmological signal (black line). Thanks to the high resolution of the NANTEN telescope the noise level is negligible in our study (magenta dash-dotted line).

logical CMB. The ICA model is given by

$$T^j(\hat{n}_i) = M_k^j S^k(\hat{n}_i), \quad (1)$$

where $T^j(\hat{n}_i)$ are the observed temperatures with the j -th band at the sky direction \hat{n}_i , M_k^j is the mixing matrix, and S^k with $k = 1, 2, 3$ are the three independent sources considered in this paper that correspond to CO, thermal dust and CMB emissions, respectively. In our simulation we consider PLANCK's $j = 100, 143$ and 217 GHz bands. The ICA algorithm estimates the sources and the mixing matrix simultaneously by maximizing the degree of non-Gaussianity of the variable Y^k with the matrix W_j^k ,

$$Y^k(\hat{n}_i) = W_j^k T^j(\hat{n}_i). \quad (2)$$

Naively, this process is equivalent to maximizing “independency” between the variables Y^k because of the central limit theorem. When the non-Gaussianity of Y^k takes the maximum, W should be M^{-1} and Y^k approaches S^k . In the present analysis we consider a noisy ICA model which is given by

$$T^j(\hat{n}_i) = M_k^j S^k(\hat{n}_i) + N^j(\hat{n}_i), \quad (3)$$

where instrumental (white) noise terms N^j are taken from the PLANCK specification (Planck Collaboration et al. 2011). Because the noise level of NANTEN telescope is not significant compared to that of the PLANCK as shown in Fig. 1, so we have neglected it.

In what follows, we use the vector notation and write T instead of T^j , etc., for clarity. Following the standard ICA procedure, we first quasi-whiten the observed data. The whitening is done by the operations (Hyvärinen 1999)

$$x(\hat{n}_i) = (T(\hat{n}_i) - \bar{T}), \quad (4)$$

$$\tilde{x}(\hat{n}_i) = (C - \Sigma)^{-\frac{1}{2}} x(\hat{n}_i), \quad (5)$$

$$\tilde{\Sigma} = (C - \Sigma)^{-\frac{1}{2}} \Sigma (C - \Sigma)^{-\frac{1}{2}}, \quad (6)$$

where $\bar{T} = E\{T\}$ is the mean of temperature in each observed band, $C = E\{xx^T\}$ is the covariance matrix of the observed

data, $\Sigma = E\{NN^T\}$ is the known noise covariance matrix, and $\tilde{\Sigma}$ is that after quasi-whitening. The ensemble average $E\{\}$ is estimated from the sample average from the observed pixels \hat{n}_i . Thus, the problem is recasted to finding a matrix W which maximizes the levels of non-Gaussianity of the variables $y \equiv W\tilde{x}$.

In the analysis we adopt the deflation algorithm, i.e., we estimate the independent components one-by-one by maximizing the non-Gaussianity of the variable $y(\hat{n}_i) = w^T \tilde{x}(\hat{n}_i)$, under a constraint $|w|^2 = 1$. In this case, the vector w^T is a row of the matrix W . To find w^T which maximizes the non-Gaussianity of the variable y , we need an evaluation function of the level of non-Gaussianity. In the present analysis we use the kurtosis as the evaluation function $g(y)$:

$$g(y) = \text{kurt}(y) = E\{y^4\} - 3(E\{y^2\})^2. \quad (7)$$

The function $g(y)$ takes the minimum $g(y) = 0$ when the variable y is Gaussian distributed. The gradient of the kurtosis is given by

$$\frac{\partial g}{\partial w} = 4E\{(w^T \tilde{x})^3 \tilde{x}\} - 12w^T (I + \tilde{\Sigma}) w (I + \tilde{\Sigma}) w, \quad (8)$$

where we have used the fact that $E\{\tilde{x}\tilde{x}^T\} = I + \tilde{\Sigma}$. In the standard gradient method, the parameter w should be updated by

$$\Delta w \propto \frac{\partial g}{\partial w} \propto E\{(w^T \tilde{x})^3 \tilde{x}\} - 3w^T (I + \tilde{\Sigma}) w (I + \tilde{\Sigma}) w. \quad (9)$$

Because we have restricted the parameter space by the constraint $|w|^2 = 1$, the vector w should satisfy the condition $w \propto \Delta w$ at the stable point. Therefore one obtains the fixed point algorithm (Hyvärinen & Oja 1997),

$$w_{\text{new}} = E\{(w^T \tilde{x})^3 \tilde{x}\} - 3w^T (I + \tilde{\Sigma}) w (I + \tilde{\Sigma}) w, \quad (10)$$

which is followed by a normalization $w_{\text{new}} \leftarrow w_{\text{new}}/|w_{\text{new}}|$. The above procedure maximizes the non-Gaussianity of the variable $y = w^T \tilde{x}$ in terms of the kurtosis.

When we need to estimate more than one independent component, we can repeat the above procedure. In this case, an orthogonalization step must be operated at every iteration before the normalization step to prevent the different vectors $w^{(n)}$ from converging to the same vector, where (n) means the n -th independent component. The orthogonalization can be done, for example, by Gram-Schmidt-like decorrelation method:

$$w^{(p+1)} = w^{(p+1)} - \sum_{j=1}^p (w^{(p+1)} \cdot w^{(j)}) w^{(j)}. \quad (11)$$

3. SKY MODEL

In Fig. 3 we show simulated sky maps at the 100, 143, and 217 GHz PLANCK bands including the CMB, foreground components and the PLANCK instrumental noises (T^j in Eq.(1)). For the CMB component we generate random Gaussian skies with the angular power spectrum consistent with the WMAP 7 year results (Larson et al. 2011). The skies are convolved with a spherical beam with the largest beam width among the three bands, namely, FWHM = 9.37 arc-min at the 100 GHz band (Planck Collaboration et al. 2011). For the instrumental noises we assume white noises for about 14

NANTEN MBM region

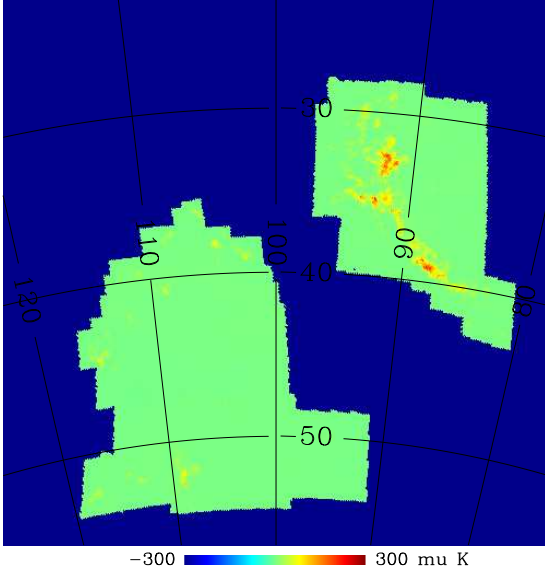


FIG. 2.— CO line emission intensity at the MBM and Pegasus region observed by NANTEN telescope. The unobserved (masked) region is shown in blue.

months observation with the amplitudes

$$\Delta T [\mu K / \text{pix}] = \Delta T [\mu K / \text{beam}] \frac{\theta_{\text{beam}}}{\theta_{\text{pix}}} = \begin{cases} 2.80 (100\text{GHz}) \\ 1.79 (143\text{GHz}) \\ 2.55 (217\text{GHz}) \end{cases} \quad (12)$$

where $\theta_{\text{pix}} = 6.87$ arc-min (Gaussian) with the HEALPIX parameter $N_{\text{side}} = 512$ (Górski et al. 2005). The noise terms N^j in Eq.(3) are realized randomly from normal distributions with variances given by Eq. (12).

For the foreground components we assume galactic thermal dust and CO line emissions. In particular, thermal dust emissions and CO line contaminations are prominent at 217 GHz and the 100 and 217 GHz bands, respectively. For the thermal dust emissions we follow the “model 8” of Finkbeiner et al. (Finkbeiner et al. 1999), which gives predictions of dust maps at microwave frequencies through extrapolations from Schlegel et al. (1998). The same model maps are implemented in a recent paper (Sehgal et al. 2010), and slightly different maps (“model 7”) are used in the PLANCK Sky Model (Delabrouille et al. 2012). For the CO line contamination at the 100 GHz band we use real data at MBM and Pegasus region observed by NANTEN telescope (Yamamoto et al. 2003, 2006) and convert the NANTEN velocity-integrated intensity map to the CMB temperature map at 100 GHz band by multiplying the conversion factor $\alpha^{J=1-0} \equiv T_{\text{CO}}^{100\text{GHz}} / I_{\text{CO}}^{J=1-0} = 14.2$ found by the PLANCK team (Planck HFI Core Team et al. 2011). The FWHM of the NANTEN beam is about 2.6 arcmin and we smooth the map to 9.37 arcmin by using the subroutine *alteralm* in the HEALPix facilities in order to match the FWHM of the PLANCK 100GHz band. While the CO line contamination at the 143 GHz band is found not to be significant (Planck HFI Core Team et al. 2011) we must taken into consideration the contamination at the 217 GHz band where

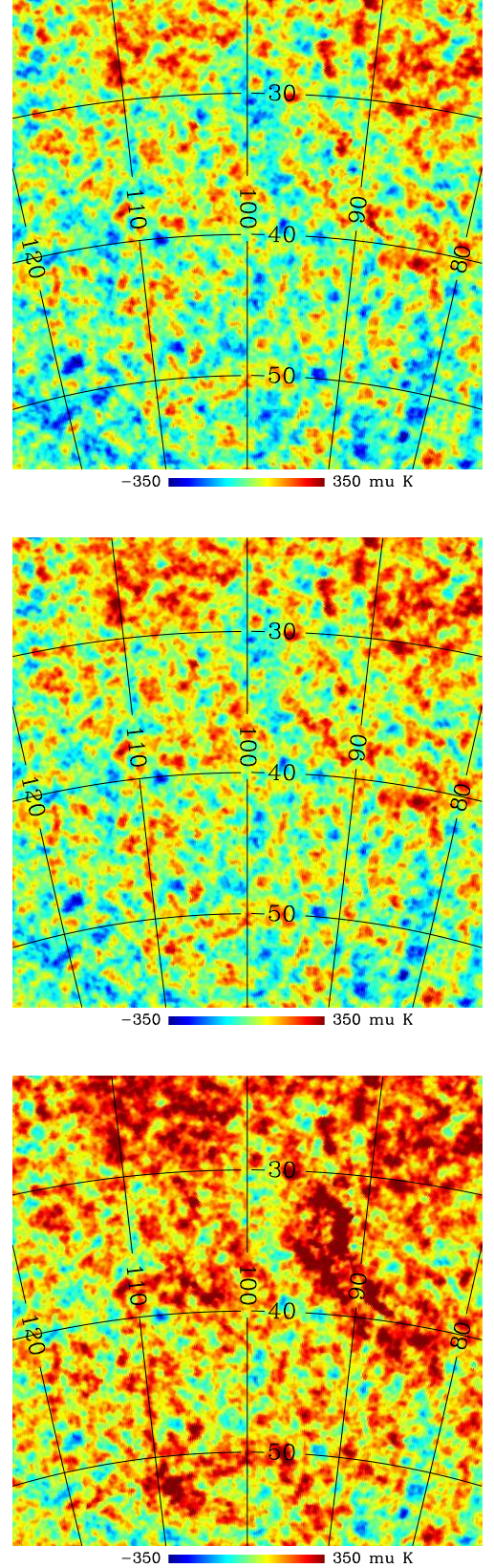


FIG. 3.— Simulated CMB sky maps at 100GHz (top), 143GHz (middle), and 217GHz (bottom).

the transition $J=(2-1)$ comes in. Because NANTEN data are not available for this transition we make a simple assumption that the intensity of $J=(2-1)$ transition is proportional to that of $J=(1-0)$.

Specifically, we make a toy sky map for the CO line emission at 217 GHz by

$$T_{\text{CO}}^{217\text{GHz}}(\hat{n}_i) = R_{J_{1-0}}^{J_{2-1}} \frac{\alpha^{J_{1-0}}}{\alpha^{J_{2-1}}} T_{\text{CO}}^{100\text{GHz}}(\hat{n}_i). \quad (13)$$

Here the integrated line ratio, $R_{J_{1-0}}^{J_{2-1}} = 0.77 \pm 0.24$, is taken from Ingalls et al. (2000), in which they estimated the ratio between $J=(4-3)$, $(2-1)$ and $(1-0)$ at high galactic molecular clouds based on the observations using the Antarctic Sub-millimeter Telescope, Remote Observatory and the Five College Radio Astronomy Observatory.

Because the CO line emission data is limited to the MBM and Pegasus region ($f_{\text{sky}} \approx 0.8\%$) shown in Fig. 2 we concentrate our analysis only for this region.

3.1. Foreground Components in the CMB angular power spectrum

We depict the angular power spectra in Fig. 4 showing the impact of the foreground components at the MBM and Pegasus region and instrumental noises on the power spectra. To estimate the power spectra we mask all the pixels outside the MBM and Pegasus region and use the Polspice code (Szapudi et al. 2001; Chon et al. 2004). Errors are estimated by generating five hundred mock CMB and instrumental white noise maps as described earlier. Because the mask covers most part of the sky ($f_{\text{sky}} \approx 0.8\%$ for the MBM and Pegasus region) and we thus have large cosmic variance errors with correlations between neighboring multipoles, we bin the spectra with the bandwidth $\Delta\ell = 25$.

It has been known that the thermal dust component has larger power at higher frequencies and affected the spectrum mainly at larger angular scales (Tegmark et al. 2000; Masi 2004). We find that this holds true for the MBM and Pegasus region considered here. On the other hand, we find that the CO component gives significant contaminations at smaller angular scales. The contamination can be larger than the instrumental and cosmic variance errors at $\ell \gtrsim 900$ and $\ell \gtrsim 400$ at the 100 and 217 GHz bands, respectively. Galactic synchrotron emissions are found to be always subdominant in those frequencies and multipole range because the MBM and Pegasus region is far away from the galactic disk, and we have omitted in our current analysis.

4. RESULTS

4.1. Foreground components estimated by the FastICA

To the sky maps prepared in the previous section we apply the FastICA algorithm in order to estimate the CO contribution and subtract it from the maps. As described earlier, we use the sky maps at three frequency bands to separate out three independent components based on the kurtosis.

In Fig. 6, the three sources obtained from the ICA algorithm are shown. We find that in our deflection algorithm, the algorithm always finds the CO-like component as the first independent component (S^1), irrespective of the initial condition for the vector w . This is caused by the fact that the distribution of the CO line intensity has the largest non-Gaussianity in terms of the kurtosis among the three component (CO, dust and CMB). It is also evident from the figure that the second

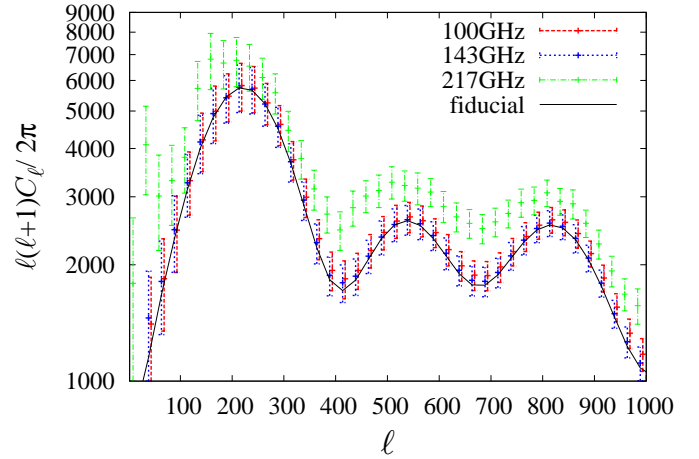


FIG. 4.— The binned power spectra and error bars estimated from 500 Monte-Carlo simulations, with foreground components and instrumental noises. For clarity, the positions of the bins for 100 and 217 GHz are shifted by $\Delta\ell = \pm 5$, respectively. The CO components affect the spectrum at small angular scales at the 100 and 217 GHz bands, while the thermal dust component dominates at large angular scales at the 217 GHz band.

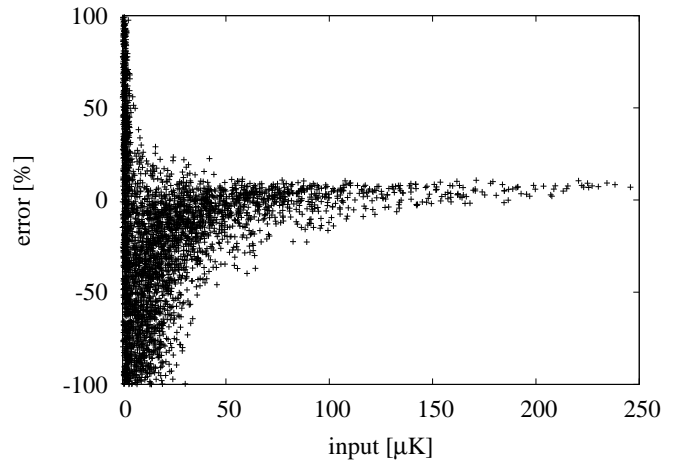


FIG. 5.— The fractional error in the estimated CO intensity at each pixel at the 100GHz band. Here the CO is assumed to be the first independent component. While the errors can be large at pixels in which the CO intensities are intrinsically small as $T_{\text{CO}} \lesssim 50\mu\text{K}$, the errors are less than 10% in pixels with large temperature in this particular realization.

independent component S^2 is most responsible for the thermal dust component given by the dust model of Finkbeiner et al..

In order to investigate the performance of the FastICA method as an estimator of the CO component we make a scatter plot as shown in Fig. 5. In the figure we show the intensity of the first independent component estimated by the FastICA at each pixel against the input CO intensity. We find that the accuracy depends on realizations; namely, on particular CMB and noise realizations on which the CO emissions are superimposed. Overall, for most of the realizations the errors can be less than $\lesssim 30\%$ at pixels where the CO emissions are strong, while the estimated intensity has large scatter where the CO intensity is intrinsically small.

Because the performance depends on realizations, we again use the Monte-Carlo simulations described earlier to rate the performance statistically as discussed below.

4.2. Angular Power Spectrum Estimation

To rate statistically the performance of the FastICA method which depends on realizations, here we apply FastICA method to all the simulated CMB maps, estimate the foreground components to be removed, and calculate the CMB angular power spectrum for each realization. The results are shown in Fig. 7. In this figure we show the power spectrum of the CMB component that is estimated as the third independent component. Clearly, it is found that the additional power due to the galactic foregrounds found in Fig. 4 is successfully removed from all the frequency bands by the ICA, and the input CMB angular power spectrum is recovered within their error bars.

Interestingly, we find that the error bars are almost unaffected by this procedure. The errors become larger only about $\lesssim 10\%$ at the 217 GHz band where the foreground contamination is the largest, while at the 100 and 143 GHz bands the error bars in the estimations of the CMB power spectra have almost the same magnitude as those before the foreground removal. The 10% increase of the errors can be considered as uncertainties in the FastICA method.

In the bottom panel of Fig. 7 we again depict the band powers normalized by the input CMB angular power spectrum. An acoustic-like structure in the estimated bias is seen; the power is underestimated around the acoustic peaks and overestimated around the dips. This is partly because we have binned the power spectrum with an equal weighting in the $\ell(\ell+1)C_\ell$ space. Note however that the bias is well within the error bars.

5. SUMMARY AND DISCUSSION

In this paper we considered the CMB foreground subtraction problem, paying particular attention to the lowest two rotational transitions of CO molecule $J=(1-0)$ and $J=(2-1)$ that contaminate the PLANCK 100 GHz and 217 GHz bands, respectively. Firstly, we estimated the angular power spectrum of the CO line emissions at the MBM and Pegasus region observed by NANTEN telescope, and found that the CO line emissions have significant contribution to the angular power spectrum especially at small angular scales ($\ell \gtrsim 900$ and 400 for the 100 and 217 GHz bands, respectively.)

The CO contamination, if it is not to be taken into account correctly, will cause a wrong estimation of cosmological parameters. In particular, the parameters related to the primordial fluctuation amplitude such as the amplitude of the curvature perturbation and its spectral index will be significantly affected. Indeed, we had found that even for a small MBM and Pegasus region the bias about the estimations of these parameters are beyond the 1σ error bars, toward larger amplitude and larger spectral index. We should stress, however, that this result holds only for the MBM and Pegasus region of the sky. It will be a future issue how large is the CO contamination to the estimation of the full sky CMB angular power spectrum.

Secondly, we applied the FastICA to the Foreground subtraction problem including the CO line emissions. The FastICA algorithm can separate the components based on the independency of the components or equivalently the level of non-Gaussianity, without any prior knowledge of distribution and frequency dependence of each foreground component. We find that CO-like component is extracted as the first independent component in our deflection algorithm as the CO distribution has the largest non-Gaussianity among the components considered here. This fact can be used to estimate quickly the CO component in the PLANCK data.

Based on the Monte Carlo simulations including CO and

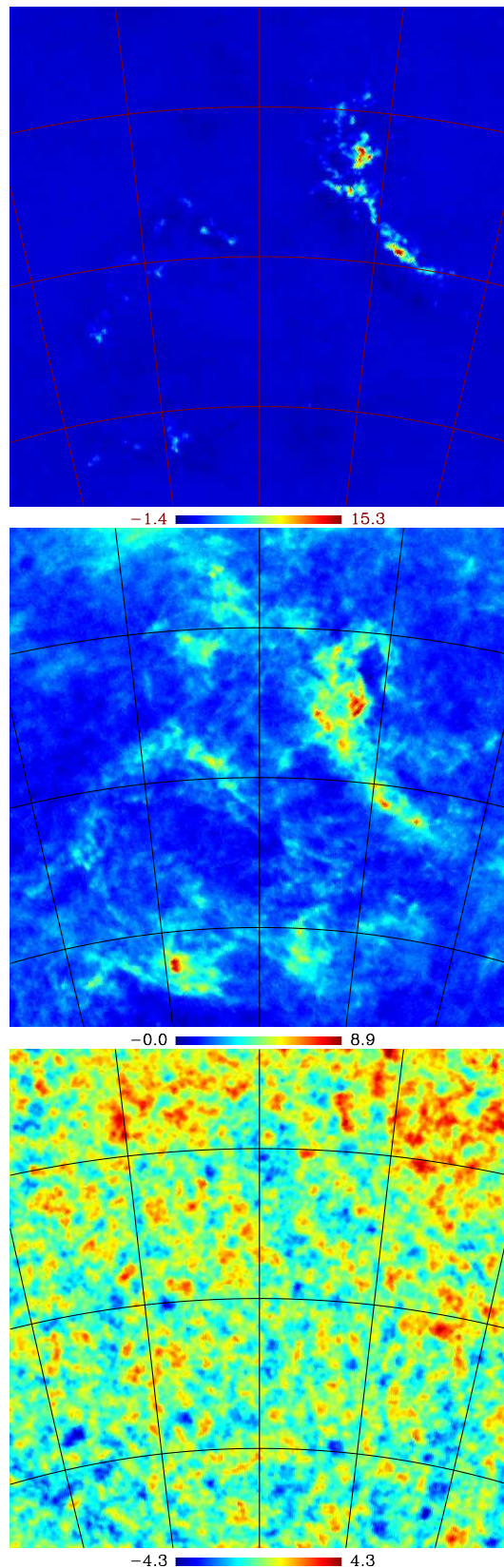


FIG. 6.— Independent components (S^1 , S^2 , and S^3) obtained from the ICA algorithm. The source with the largest non-Gaussianity is shown in the top panel and the smallest in the bottom. It is clear that the ICA successfully estimates the CO distribution (S^1) in the top panel. The second source seems to be thermal dust emissions. The amplitudes are arbitrary because of the degeneracy between the sources and mixing matrix components.

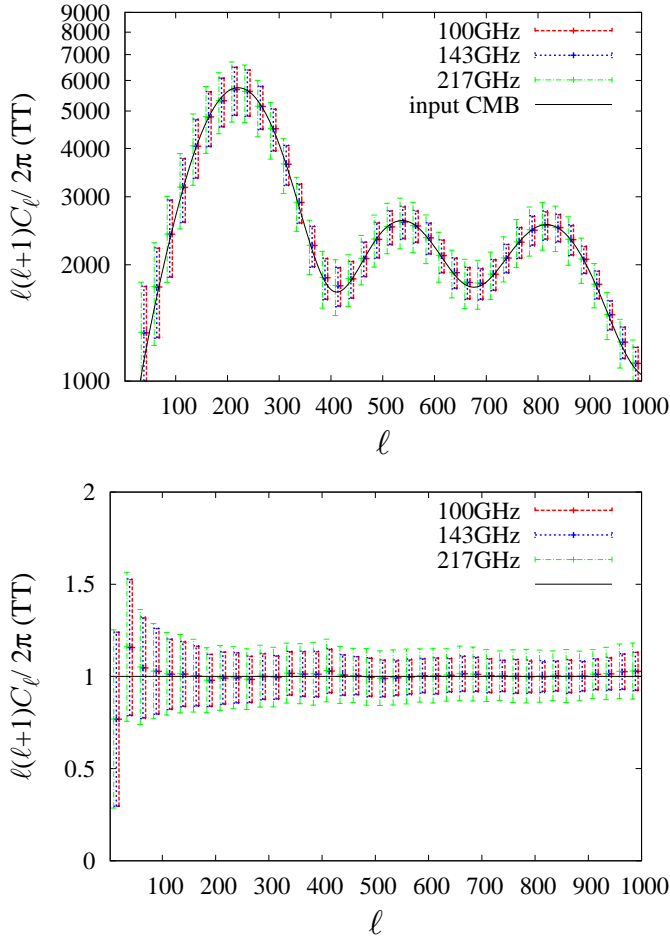


FIG. 7.— The binned power spectrum and error bars estimated from 500 Monte-Carlo simulations (top) and fractional errors (bottom). For clarity, the positions of the bins for 100 and 217 GHz are shifted by $\Delta\ell = \pm 5$, respectively. Acoustic structure in the estimated bias is seen; the power is underestimated around the acoustic peaks and overestimated around the dips. However, the bias is well within the error bars.

thermal dust emissions as foregrounds, we investigated how the CMB is recovered in terms of the power spectrum. Though the accuracy depends on the particular realization of the instrumental noises and CMB, we found that the recovery is very well in statistical sense. The success is thanks to the approximate statistical independence between the foreground components like CO and background CMB. This is consistent with the result in the earlier literature where the authors applied the FastICA method to the WMAP data and found that it can recover the CMB angular power spectrum consistent with the spectrum independently derived by the WMAP team (Maino et al. 2007).

Finally, we should comment on the impact of the FastICA method on the level of non-Gaussianity in the estimated CMB map. Because the method relies on the non-Gaussianity to estimate the independent components, naively it should affect the non-Gaussianity of the CMB which probably has the smallest degree of non-Gaussianity among the components in

the microwave sky. In Fig. 8, we show the kurtoses in the estimated CMB (red) and CMB+Foreground (blue) maps against the value in the input CMB maps at the 217 GHz band in the MBM and Pegasus region. Clearly, it is seen that the bulk of the kurtosis which comes from the thermal dust and CO components is removed through the method. Interestingly, we find that some portion of the kurtosis in the CMB maps (which should be zero in the mean in our Gaussian simulation) is recovered with a scatter about 20% when the kurtosis has large value ($|\text{kurt}| \gtrsim 0.2$). However, the accuracy depends on the size of the kurtosis, and the method induces a false signal of the kurtosis in the estimated CMB map when the input kurtosis is too small. We leave this issue for future investigation.

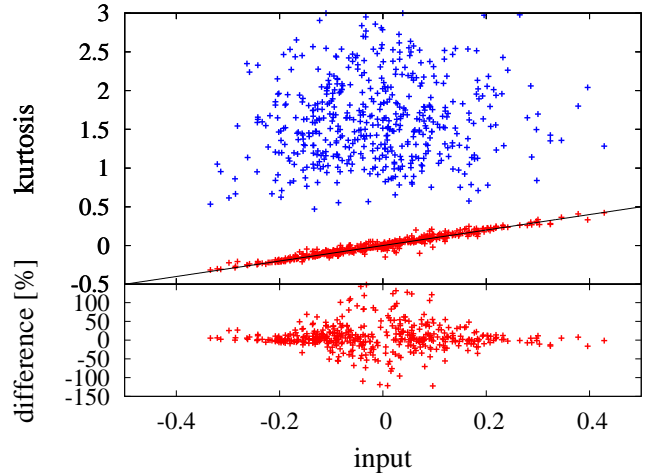


FIG. 8.— (Top) Kurtoses in the estimated CMB (red) and CMB+Foreground (blue) maps at the 217 GHz band. The straight line represents linear relation. (Bottom) Fractional differences between the input and estimated kurtoses.

In conclusion, in this paper we found that the FastICA can efficiently extract the CO line foregrounds that contaminate the PLANCK HFI bands. The method will be useful to estimate the CO distribution in the real PLANCK data, and any foreground component whose distribution is not known in advance in the future CMB experiments.

One of the authors (KI) would like to thank T. Matsumura, E. Komatsu, and O. Doré for helpful comments and useful discussions. KI also thanks A. Asai for her kind support on the IDL manipulation. This work has been supported in part by Grant-in-Aid for Scientific Research Nos. 24340048 (KI), 22740119 (HY), 23340046, 24111707 (TTT), and 24224006 (YF) from the Ministry of Education, Sports, Science and Technology (MEXT) of Japan, and by Grant-in-Aid for the Global Center of Excellence program at Nagoya University "Quest for Fundamental Principles in the Universe: from Particles to the Solar System and the Cosmos" from the MEXT of Japan. The work has also been supported by the Strategic Young Researcher Overseas Visits Program for Accelerating Brain Circulation Nos. R2405 (TTT) and R2211 (YF) commissioned by JSPS.

REFERENCES

Bennett, C. L. et al. 1996, *ApJ*, 464, L1, arXiv:astro-ph/9601067
 Bonaldi, A., Bedini, L., Salerno, E., Baccigalupi, C., & de Zotti, G. 2006, *MNRAS*, 373, 271, arXiv:astro-ph/0609701

Bottino, M., Banday, A. J., & Maino, D. 2010, *MNRAS*, 402, 207, 0910.4405
 Chapman, E. et al. 2012, *MNRAS*, 423, 2518, 1201.2190

- Chon, G., Challinor, A., Prunet, S., Hivon, E., & Szapudi, I. 2004, *MNRAS*, 350, 914, arXiv:astro-ph/0303414
- Dame, T. M., Hartmann, D., & Thaddeus, P. 2001, *ApJ*, 547, 792, arXiv:astro-ph/0009217
- Delabrouille, J. et al. 2012, *ArXiv e-prints*, 1207.3675
- Donzelli, S. et al. 2006, *MNRAS*, 369, 441, arXiv:astro-ph/0507267
- Dunkley, J. et al. 2009, in *American Institute of Physics Conference Series*, Vol. 1141, American Institute of Physics Conference Series, ed. S. Dodelson, D. Baumann, A. Cooray, J. Dunkley, A. Fraisse, M. G. Jackson, A. Kogut, L. Krauss, M. Zaldarriaga, & K. Smith, 222–264, 0811.3915
- Efstathiou, G., Gratton, S., & Paci, F. 2009, *MNRAS*, 397, 1355, 0902.4803
- Eriksen, H. K., Banday, A. J., Górski, K. M., & Lilje, P. B. 2004, *ApJ*, 612, 633, arXiv:astro-ph/0403098
- Finkbeiner, D. P., Davis, M., & Schlegel, D. J. 1999, *ApJ*, 524, 867, arXiv:astro-ph/9905128
- Górski, K. M., Hivon, E., Banday, A. J., Wandelt, B. D., Hansen, F. K., Reinecke, M., & Bartelmann, M. 2005, *ApJ*, 622, 759, arXiv:astro-ph/0409513
- Hobson, M. P., Jones, A. W., Lasenby, A. N., & Bouchet, F. R. 1998, *MNRAS*, 300, 1, arXiv:astro-ph/9806387
- Hyvärinen, A. 1999, *IEEE Signal Processing Letters*, 6, 145
- Hyvärinen, A., & Oja, E. 1997, *Neural Computation*, 9, 1483
- Ingalls, J. G., Bania, T. M., Lane, A. P., Rumitz, M., & Stark, A. A. 2000, *ApJ*, 535, 211, arXiv:astro-ph/9912079
- Katayama, N., & Komatsu, E. 2011, *ApJ*, 737, 78, 1101.5210
- Komatsu, E. et al. 2011, *ApJS*, 192, 18, 1001.4538
- Larson, D. et al. 2011, *ApJS*, 192, 16, 1001.4635
- MacTavish, C. J. et al. 2006, *ApJ*, 647, 799, arXiv:astro-ph/0507503
- Maino, D., Banday, A. J., Baccigalupi, C., Perrotta, F., & Górski, K. M. 2003, *MNRAS*, 344, 544, arXiv:astro-ph/0303657
- Maino, D., Donzelli, S., Banday, A. J., Stivoli, F., & Baccigalupi, C. 2007, *MNRAS*, 374, 1207
- Maino, D. et al. 2002, *MNRAS*, 334, 53, arXiv:astro-ph/0108362
- Masi, S. 2004, *Advances in Space Research*, 34, 483
- Mizuno, A., & Fukui, Y. 2004, in *Astronomical Society of the Pacific Conference Series*, Vol. 317, *Milky Way Surveys: The Structure and Evolution of our Galaxy*, ed. D. Clemens, R. Shah, & T. Brainerd, 59
- Onishi, T., Yoshikawa, N., Yamamoto, H., Kawamura, A., Mizuno, A., & Fukui, Y. 2001, *PASJ*, 53, 1017
- Planck Collaboration et al. 2011, *A&A*, 536, A1, 1101.2022
- Planck HFI Core Team et al. 2011, *A&A*, 536, A6, 1101.2048
- Schlegel, D. J., Finkbeiner, D. P., & Davis, M. 1998, *ApJ*, 500, 525, arXiv:astro-ph/9710327
- Sehgal, N., Bode, P., Das, S., Hernandez-Monteagudo, C., Huffenberger, K., Lin, Y.-T., Ostriker, J. P., & Trac, H. 2010, *ApJ*, 709, 920, 0908.0540
- Szapudi, I., Prunet, S., & Colombi, S. 2001, *ApJ*, 561, L11
- Tauber, J. A. et al. 2010, *A&A*, 520, A1
- Tegmark, M., Eisenstein, D. J., Hu, W., & de Oliveira-Costa, A. 2000, *ApJ*, 530, 133, arXiv:astro-ph/9905257
- Yamamoto, H., Kawamura, A., Tachihara, K., Mizuno, N., Onishi, T., & Fukui, Y. 2006, *ApJ*, 642, 307, arXiv:astro-ph/0601315
- Yamamoto, H., Onishi, T., Mizuno, A., & Fukui, Y. 2003, *ApJ*, 592, 217